Observations and Modeling of the August 27, 2012 Earthquake and Tsunami affecting El Salvador and Nicaragua

Jose C. Borrero,[1,2] Nikos Kalligeris,[2] Patrick J. Lynett,[2] Hermann M. Fritz,[3] Andrew V. Newman,[4] and Jaime A. Convers[4]

Abstract—On 27 August 2012 (04:37 UTC, 26 August 10:37 p.m. local time) a magnitude $M_w = 7.3$ earthquake occurred off the coast of El Salvador and generated surprisingly large local tsunami. Following the event, local and international tsunami teams surveyed the tsunami effects in El Salvador and northern Nicaragua. The tsunami reached a maximum height of ~ 6 m with inundation of up to 340 m inland along a 25 km section of coastline in eastern El Salvador. Less severe inundation was reported in northern Nicaragua. In the far-field, the tsunami was recorded by a DART buoy and tide gauges in several locations of the eastern Pacific Ocean but did not cause any damage. The field measurements and recordings are compared to numerical modeling results using initial conditions of tsunami generation based on finite-fault earthquake and tsunami inversions and a uniform slip model.

1. Introduction

Situated along a major subduction zone plate boundary, the Pacific coast of Central America (Fig. 1) is vulnerable to near-field, regional, and far-field tsunamis (Fernandez *et al.* 2004; Álvarez-Gómez *et al.* 2013), with risk dependent strongly on coastal exposure and population. The US National Geophysical Data Center World Data Service for Geophysics (NGDC/WDS) database lists 21 tsunami events affecting El Salvador and seven events

[1] eCoast Ltd., 47 Cliff St., Raglan 3225, New Zealand. E-mail: jose@ecoast.co.nz

[2] Tsunami Research Center, Sonny Astani Department of Civil and Environmental Engineering, University of Southern California, Los Angeles, CA 90089, USA.

[3] School of Civil and Environmental Engineering, Georgia Institute of Technology, Atlanta, GA 30322, USA.

[4] School of Earth and Atmospheric Sciences, Georgia Institute of Technology, Atlanta, GA 30332, USA.

affecting Nicaragua. While there are several older events with questionable validity, it is clear that these countries have been affected by tsunamis in the past. Notable events in El Salvador prior to 2012 include near-field tsunamis in 1859 ($M_l \sim 7.6$; White *et al.* 2004) and 1902 (no observed earthquake shaking; White *et al.* 2004), the latter of which reportedly caused 185 deaths in the western portion of the country; however, this event is questionable and may have been meteorological in origin. Regional sources, such as the 1906 Ecuador earthquake (Kelleher 1972), have also caused tsunamis affecting El Salvador. Damaging tsunami waves were reported as a result of the 9 March 1957 earthquake in the Aleutian Islands, which reportedly caused deaths and damage in Acajutla (Fernandez *et al.* 2004), although this death toll is not reflected in the NGDC database. Non-damaging tsunami waves were also observed from other major transpacific tsunamis such as the 1960 and 2010 tsunamis from Chile and the 2011 Tohoku, Japan, tsunami. Nicaragua on the other hand, has scant reports of effects from far-field tsunamis. Nicaragua is best known for the tsunami of 2 September 1992, which is particularly notable in that it was caused by a slow earthquake with moment magnitude, M_w 7.7 (Kanamori and Kikuchi 1993). That tsunami had a maximum run-up height of ~ 10 m and caused 170 deaths and USD $30 million in damage (Abe *et al.* 1993; Satake *et al.* 1994).

2. Earthquake Details

On 26 August 2012 at 10:37 p.m. local time (27 August 2012, 0437 UTC), an earthquake with M_w 7.3 (W-phase) occurred off the coast of El Salvador and
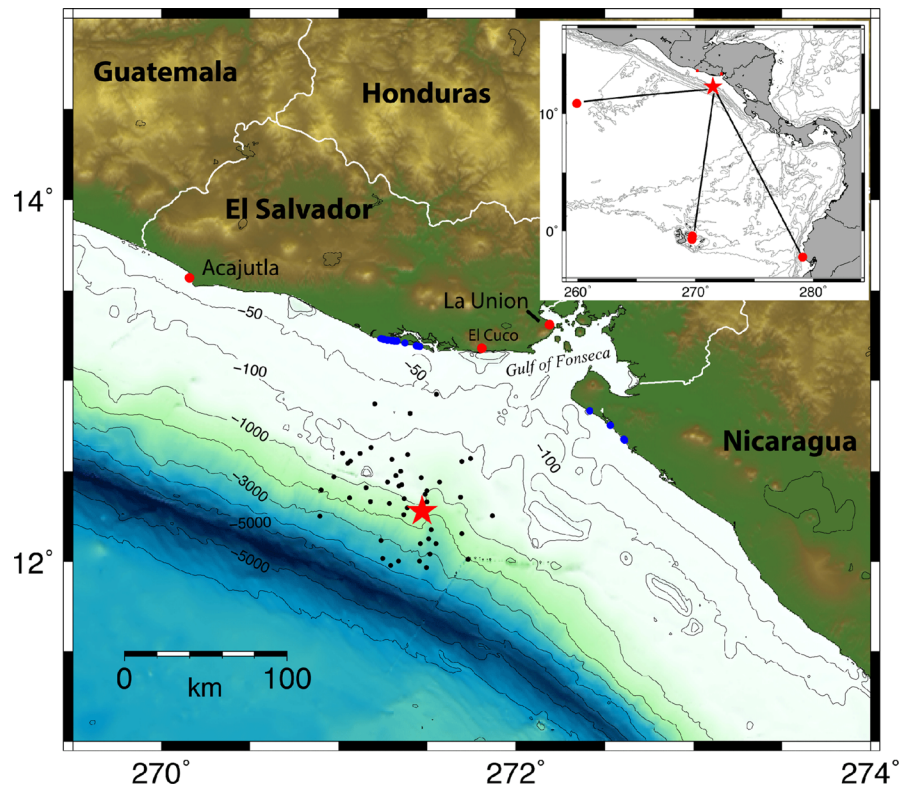
Figure 1

The offshore bathymetry of El Salvador and northern Nicaragua, and the location of the USGS-defined earthquake epicenter (*red star*). *Black dots* correspond to epicenters of aftershocks through 11 September 2012. Depth *contours* labeled in meters. *Blue dots* are locations where tsunami field data were recorded (inset map). Location of El Salvador and the earthquake epicenter relative to (from west to east) Deep-ocean Assessment and Reporting of Tsunamis (DART) tsunameter 43413 and the Galapagos Islands and La Libertad, Ecuador tide gauge stations (*red dots*)

Nicaragua. The epicenter, as reported by the US Geological Survey (USGS), was located approximately 75 km due south of the El Salvador coastline (Fig. 1). Approximately 50 aftershocks with magnitudes between 5.5 and 4.2 occurred in the vicinity of the main event between 27 August and 11 September 2012. The initial assessment of the earthquake by the Pacific Tsunami Warning Center (PTWC) determined that the earthquake was significant due to the strength of the seismic signal and the long-period nature of the initial seismic waves. Within 10 min of the main shock, additional analysis by the PTWC suggested that the earthquake could be characterized as a 'slow' earthquake. This was indicated by Θ ($=\log_{10}(E/M_0)$) values (NEWMAN and OKAL 1998) in the range of -6.5 to -6.0 as computed by the PTWC. Typical values of Θ for 'typical' thrust earthquakes are generally larger, in the range of -4.7. Additionally, Θ values

derived by the West Coast Alaska Tsunami Warning Center (WCATWC) were even lower at -7.0, further suggesting a very slow event. Analysis provided by the Real-Time Earthquake Energy and Rupture Duration project at the Georgia Institute of Technology also identified the event as slow and 'weak' 11 min after the initiation of the main shock.

3. Deficiency in Radiated Seismic Energy

Following BOATWRIGHT and CHOY (1986), and with corrections for real-time implementation by NEWMAN and OKAL (1998), both the radiated seismic energy and rupture durations of global earthquakes since 1997 with $M_w > 6.7$ have been estimated by CONVERS and NEWMAN (2011). Events since early 2009 were analyzed using a set of programs called 'RTerg'
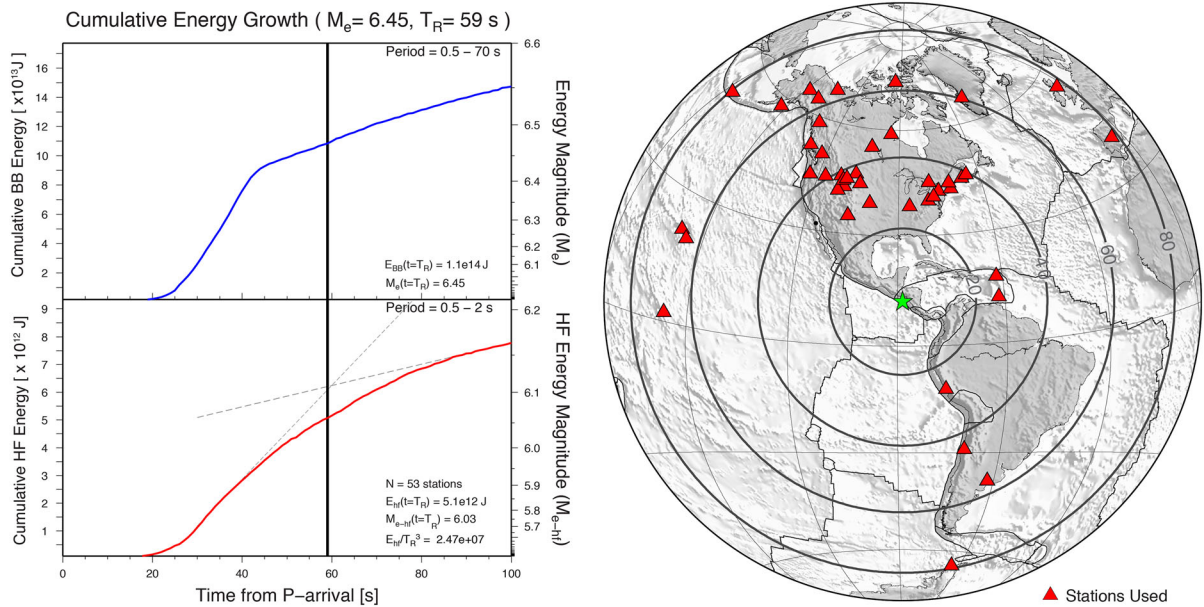
Figure 2

(*left*) Cumulative energy in broadband (0.5–70 s top trace, *blue*) and high-frequency (period 0.5–2 s, *bottom* trace, *red*) energy. The high-frequency energy is used to approximate T_R and evaluate the broadband energy E following CONVERS and NEWMAN (2011). (*right*) Teleseismic stations between 25° and 80° used to calculate the radiated seismic energy

(NEWMAN *et al*. 2011). The results of broadband energy, high-frequency energy, and rupture duration (Fig. 2) help to characterize strong shaking and tsunami potential, especially in the case of tsunami earthquakes, which are identified as being deficient at radiating seismic energy (KANAMORI 1972). Using the energy-to-moment ratio parameter as a discriminant for tsunami earthquakes (NEWMAN and OKAL 1998), such events can be identified by their low Θ value, thereby qualifying them as tsunami earthquakes (NEWMAN and OKAL 1998; CONVERS and NEWMAN 2011). While most events have a Θ value between −4.0 and −5.0, slow tsunami earthquakes have Θ ≤ − 5.7 (NEWMAN and OKAL 1998). The El Salvador earthquake, with a radiated energy of 1.1×10^{14} J (Fig. 2), released about 25 times less seismic energy than other earthquakes of the same size, and showed an energy-to-moment value of Θ = −6.0 (Fig. 2), clearly lower than average and classifying it as a slow-rupturing tsunami earthquake.

The observed rupture duration (T_R) of 59 s was approximately three times longer than expected using a typical duration-cubed scaling relationship with seismic moment (HOUSTON 2001). The extended duration, unlike other earthquakes of the same

magnitude, is typical of slow-source tsunami earthquakes, along with their deficient rupture high-frequency energy. The threshold of $E_{hf}/T_R^3 < 5 \times 10^7$ J/s, is also used as a discriminator for tsunami earthquakes (NEWMAN *et al*. 2011, Fig. 3), where, similar to other tsunami earthquakes, the El Salvador event stands out with an anomalous T_R and deficiency in its radiated high-frequency energy (E_{hf}). Individuals in the area at the time of the earthquake described the ground shaking as 'light', a feature that corroborates the seismologic evidence for a slow rupture. Such was the case for the 1992 Nicaragua event and other tsunami earthquakes, where many who felt the event thought the earthquake was considerably smaller and less dangerous than it actually was (e.g. KANAMORI 1972; KANAMORI and KIKUCHI 1993; SATAKE *et al*. 1994; HILL *et al*. 2012).

4. Summary of Tsunami Effects

The earthquake generated a moderate tsunami observed by eyewitnesses and instruments located in both the near field (Acajutla and La Unión) and far field (Baltra and Santa Cruz, Galapagos Islands; La
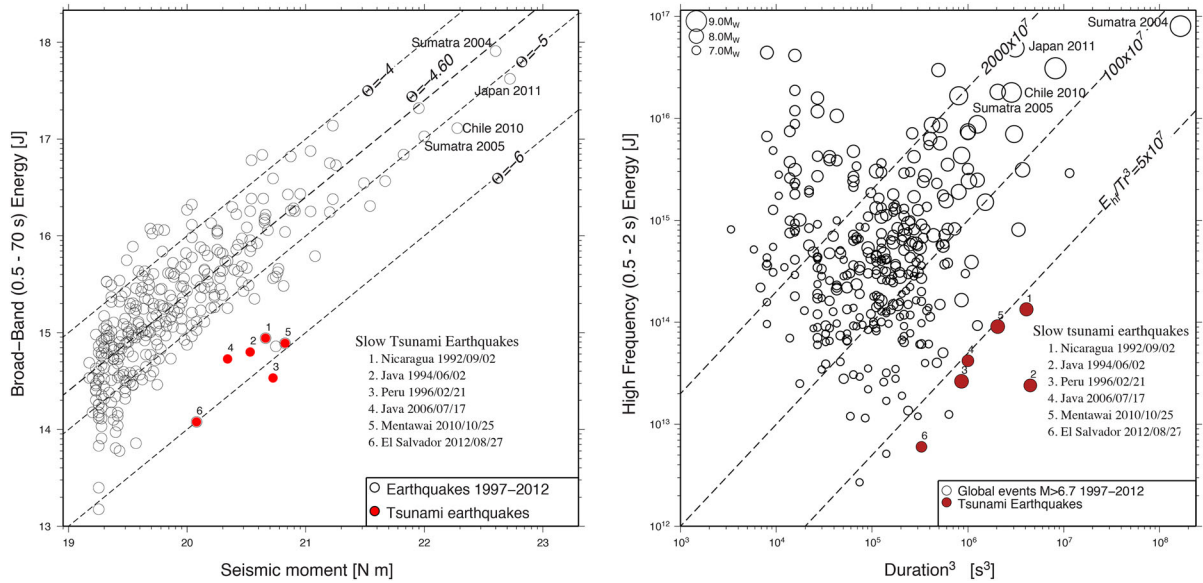
Figure 3

(*left*) Global energy-to-seismic moment comparison for earthquakes greater than M_w 6.7. The *dashed line* represents the global average and constant values of the energy-to-moment ratio ($\log_{10} E/M_0$) (NEWMAN and OKAL 1998). Energy-deficient earthquakes tend to the *bottom right*, while strong-rupturing earthquakes tend to the *top left*. Highlighted are known and identified tsunami earthquakes (events of this type before 1997 are from CONVERS and NEWMAN (2011) and are included for comparison). (*right*) Relationship between high-frequency energy and the cube of the duration for the same dataset; earthquakes with low radiated high-frequency energies and disproportional long durations are grouped in the *bottom right*

Table 1

PTWC Summary of tide gauge recordings from the El Salvador tsunami

Station	Country	Lat. (°)	Long. (°)	Arrival (hours)	Z2P (m)	P2T (m)	Period (mm:ss)
Acajutla	El Salvador	13.57	−89.84	0:52	0.11	0.21	8:00
DART 43413	n/a	10.84	−100.08	1:36	0.01	0.02	8:00
La Unión	El Salvador	13.31	−87.81	1:40	0.03	0.04	9:00
Baltra	Ecuador (Galapagos Is)	−0.44	−90.28	2:30	0.35	0.70	10:00
Santa Cruz	Ecuador (Galapagos Is)	−0.72	−90.31	2:49	0.22	0.39	13:20
La Libertad	Ecuador	−2.22	−80.91	3:36	0.21	0.37	11:30

Z2P zero-to-peak wave amplitude, *P2T* peak-to-trough wave height

Libertad, Ecuador; Easter Island; and DART station 43413, see Fig. 1). A summary of water level measurements provided by the PTWC shortly after the event is provided in Table 1. Due to the location of the earthquake and the fact that tsunamis primarily radiate wave energy perpendicular to the trench axis, the tide gauge in Acajutla was not ideally located to receive the direct tsunami signal, while El Salvador's other tide gauge at La Unión is located several kilometers from the open ocean in the shallow and sheltered Gulf of Fonseca (Fig. 1). In contrast, the

Galapagos Islands situated approximately 1,400 km away along a 190° (SSW) path from the source region (Fig. 1) are ideally located to receive a strong tsunami signal. As a result, the two stations in the Galapagos recorded a very strong, clear tsunami that arrived approximately 2.5 h after the earthquake. Following the initial wave packet, both stations also responded with a secondary (and in the case of Santa Cruz, a tertiary) wave packet with amplitudes nearly as large as the initial wave. A similar extended duration and resurgence of wave height was also

observed on these stations during the 11 March 11 2011 Tohoku tsunami (LYNETT et al. 2013). Located farther off-axis from the main beam of tsunami energy propagation were DART 43413 (1,200 km at 264°, see Fig. 1), which recorded a single tsunami wave pulse with a peak-to-trough (P2T) height of 0.024 m, and the La Libertad, Ecuador station (1,800 km at 153°, see Fig. 1) characterized by long-period non-tsunami oscillations present before the tsunami arrival. The tsunami itself appears clearly some 3.5 h after the earthquake, with the largest signal occurring some 5 h after the tsunami arrival. Additional details of these tsunami records, including detailed spectral analysis, are discussed in HEIDAR-ZADEH and SATAKE (2014).

In the days immediately following the event, representatives from El Salvador's Ministry for the Environment and Natural Resources (MARN) conducted an initial survey of the tsunami-affected area focused on attending to immediate needs and disseminating information to local residents. This was followed by the International Tsunami Survey Team (ITST), which visited the affected areas of El Salvador on 5–7 September 2012 and collected the majority of the quantitative data. A third survey

subsequently visited sites in northern Nicaragua in response to reports of moderate tsunami inundation occurring in several coastal villages. A detailed description of these surveys is available in BORRERO (2012) and is provided as supplementary material.

During the ITST survey, the team visited 11 separate sites, focusing primarily on the San Juan del Gozo Peninsula (Fig. 4), and recording measurements of tsunami height, run-up height, flow direction, and inundation distance using established protocols (SYNOLAKIS and OKAL 2005; UNESCO 2013). Measured data are presented relative to the tide level at the time of tsunami arrival (Fig. 4; Table 2) and are divided into flow depths, tsunami heights, and run-up heights. Because the topography landward of the dune ridge sloped downward, run-up heights are generally lower than the maximum tsunami heights.

The strongest tsunami effects were experienced along the central section of the San Juan del Gozo Peninsula. At the time of the earthquake (~10:37 p.m.) it was relatively dark with a quarter moon low over the horizon and a moonset near 1 a.m. The earthquake occurred just after high tide when scores of people were present on the beach collecting
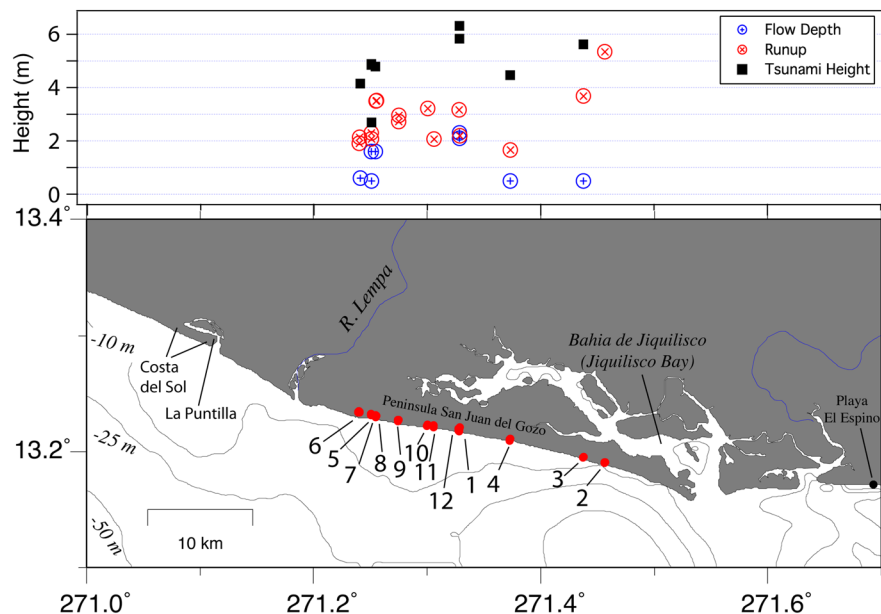

Figure 4
Summary of data collected during the ITST field survey. (lower panel) Map showing the survey locations, (upper panel) measured tsunami data broken down into run-up, flow depth, and tsunami height values

Table 2

Tsunami field data measurements from the 2012 tsunami affecting El Salvador and Nicaragua

Site	Lat. (°N)	Long (°E)	Terrain z (m)	Flow Depth h (m)	Tsunami height z + h (m)	Run-up R (m)	Distance (m)	Watermark	Description
El Salvador									
1	13.2183	−88.6716	4.2	2.1	6.3	–	82.0	Mud line inside	Eyewitness confirmed house pole
1	13.2186	−88.6716	3.5	2.3	5.8	–	121.6	Broken branch	Eyewitness confirmed wrapped in sheet metal
1	13.2206	−88.6713	2.2	–	–	2.2	340.9	Wrack line	Eyewitness confirmed
2	13.1907	−88.5433	5.3	–	–	5.3	45.8	Wrack line	Eyewitness confirmed on top of dune tree log
3	13.1950	−88.5623	5.1	0.5	5.6	–	45.9	Eyewitness	Dune overtopped ($h = 0.5$ m guessed) eyewitness confirmed
3	13.1953	−88.5622	3.7	–	–	3.7	83.9	Wrack line	Eyewitness confirmed brown grass
4	13.2101	−88.6270	4.0	0.5	4.5	–	96.4	Damaged trim line	Wooden palm leaf hut
4	13.2107	−88.6268	1.7	–	–	1.7	155.5	Wrack line	Wrack line
5	13.2315	−88.7495	3.2	1.6	4.8	–	46.0	Damaged trim line	Hut with sheet metal eyewitness confirmed Manglaron Monte Alto
5	13.2315	−88.7495	3.3	1.6	4.9	–	46.0	Damaged trim line	House siding eyewitness confirmed
5	13.2319	−88.7494	2.2	0.5	2.7	–	85.1	Raft debris	Debris in fence
5	13.2325	−88.7494	2.3	–	–	2.3	150.6	Wrack line	Brown vegetation eyewitness confirmed
5	13.2325	−88.7493	2.1	–	–	2.1	153.5	Wrack line	Brown vegetation eyewitness confirmed
6	13.2339	−88.7593	3.5	0.6	4.1	–	37.2	Damaged trim line	Hut with sheet metal eyewitness
7	13.2348	−88.7600	2.1	–	–	2.1	115.6	Wrack line	Embankment next to mangroves
7	13.2349	−88.7600	1.9	–	–	1.9	119.1	Wrack line	Wrack line next to mangroves
8	13.2305	−88.7458	3.2	1.6	4.8	–	92.1	Broken branch	Tree on top of dune
8	13.2310	−88.7447	3.5	–	–	3.5	139.9	Wrack line	Field next to fence
8	13.2310	−88.7453	3.5	–	–	3.5	141.2	Wrack line	Field next to fence
9	13.2274	−88.7252	3.0	–	–	3.0	164.7	Wrack line	
9	13.2274	−88.7253	2.7	–	–	2.7	165.7	Wrack line	
10	13.2234	−88.6997	3.2	–	–	3.2	170.4	Wrack line	Brown vegetation eyewitness confirmed
11	13.2226	−88.6941	2.1	–	–	2.1	204.2	Wrack line	Brown vegetation eyewitness confirmed
12	13.2198	−88.6720	3.2	–	–	3.2	242.9	Wrack line	Brown vegetation eyewitness confirmed
Nicaragua									
1	12.833	−87.583		0.5	–	–	106.0	n/a	n/a
2	12.672	−87.387		n/a	–	–	0.0	n/a	n/a
3	12.657	−87.376		0.5	–	–	120.0	n/a	n/a

sea turtle eggs for conservation projects. A worker at one of the hatcheries was in a ramada (a small shed with wooden posts, and walls and roof made from aluminum siding) located on the beach at the crest of the dunes approximately 70 m from the water when the earthquake occurred. This witness came out of the ramada when he heard people crying out and was subsequently caught in the wave and dragged some 90 m inland where he was ultimately suspended in a tree branch at a height of 2.1 m above the ground. This witness reported that there were three tsunami waves and that the flow depth at the ramada was just below the roof (approx. 2.5 m). During the tsunami, the walls of the ramada were torn off of the posts that are deeply embedded in the sand; the posts themselves were not pulled out of the ground, but some were pushed over by the force of the water. Other witnesses related similar stories, and in total there were more than 40 injured people, with three injuries requiring medical attention.

The effects of the tsunami along the San Juan del Gozo peninsula were relatively uniform along 25 km of mostly undeveloped coastline (Fig. 5). It is important to point out that significant tsunami effects appear to be constrained to this area. During the initial survey by MARN, the more developed tourist area of Costa del Sol some 10 km to the west did not report any inundation or wave activity. This was even true at La Puntilla, a dense cluster of several waterfront restaurants at the eastern end of the Costa del Sol sand spit. These restaurants are regularly affected by high tides (Fig. 5), however, the tsunami did not cause any damage or noticeable effects here. Individuals in other parts of El Salvador were interviewed by telephone and did not report any significant tsunami activity. At Playa El Espino (Fig. 4), a local resident and beachfront restaurant owner reported that there were no observable tsunami effects and that the local police had moved into the peninsula of San Juan del Gozo to help assist people affected in that area. Farther east at Playa

Figure 5
Images from the post-event field survey. *Clockwise* from *top left* tsunami flow depths indicated by broken branches and by an eyewitness. The vulnerable structures at La Puntilla and Costa del Sol were not affected by the tsunami. Inundation extent was clearly visible from the air and in debris *lines* on the ground. The aerial perspective also revealed evidence of sand deposition by tsunami overwash

El Cuco (Fig. 1), beachfront hotel workers did not report any tsunami activity. Local boat captains said that the boats left parked on the beach overnight were not noticeably moved or disturbed in any way and that activities of the next day resumed normally. In Nicaragua, a survey team recorded tsunami effects at three seaside villages (Fig. 1) where the tsunami caused mild inundation and flow depths on the order of 0.5 m (Norwin Acosta, *pers. comm.* report included in supplementary material).

5. *Tsunami Modeling*

We modeled the tsunami propagation and inundation using the MOST suite of integrated numerical codes capable of simulating tsunami generation, transoceanic propagation, and its subsequent inundation in the coastal area (Titov 1997). The model uses a finite-difference numerical scheme to solve the $2 + 1$ nonlinear shallow-water (NSW) equations in characteristic form, accounting for nonlinearity, but not for frequency dispersion. NSW calculations are extended using a moving boundary for run-up and inundation on the dry bed, and bottom friction is included. The bathymetry used for the modeling grids was derived from the relatively coarse GEBCO 30-s global bathymetry and topography data. The offshore bathymetry of the tsunami-affected area was manually adjusted to remove a large-scale bathymetric depression situated directly offshore of the survey site that does not appear on local navigational charts. Four levels of nested grids of sequentially finer resolution (300, 100, 50, and 10 m) were used for the near-field model. A fifth grid at approximately 900-m resolution was created to assess the far-field propagation of the tsunami. Models of co-seismic slip along the earthquake fault were converted to sea floor deformation through the method of Okada (1985) and implemented as an initial condition by translating the instantaneous static deformation to the sea surface.

6. *Tsunami Source Models*

We developed a suite of eight tsunami source models to initialize the hydrodynamic computation

Table 3

General description and characteristics of the different source models

Source	Details
S1	USGS finite fault model, no scaling
S2	USGS finite fault model, 1.92 scale factor based on a slow rupture in mechanically softer material (see Newman *et al.* 2011 and "Appendix" section)
S3	USGS finite fault model, 2.55 scale factor to match amplitude of leading wave at DART 43413
S4	Moment magnitude-constrained custom inversion based on a least-squares regression between modeled tsunami waveforms produced by unit (1 m) slip on shallow subfaults in the source region and recorded data at DART 43413
S5	Same as 4, but magnitude is unconstrained
S6	Rectangular fault model. 60 × 30 km, 2.2 m slip, dip 15°, rake 81°, strike 287°, determined from macro-scale seismic parameters (Heidarzadeh and Satake 2014)
S7	Ye *et al.* (2013) finite fault model, no scaling ($V_r = 2.0$ km/s)
S8	Ye *et al.* (2014) finite fault model, with modified rupture velocity ($V_r = 1.5$ km/s)

(Table 3). Five sources were based on teleseismic inversions, two sources were based on a hydrodynamic inversion of the DART water level signal and one source was based on earthquake magnitude and assumed rupture extents. For the first three models, we used the finite-fault model of Ji *et al.* (2002), as reported by the US Geological Survey shortly after the event (USGS 2012). Source 1 used the unscaled slip distribution across a source area of 210 × 128 km with a maximum slip amount of approximately 1 m. Strike and dip angles of the fault were fixed to 296° and 16°, respectively, and the rake angle is variable. For Source 2, we scaled the teleseismically-determined slip distribution by a uniform factor of 1.92 using the approach of Newman *et al.* (2011) in their modeling of the 2010 Mentawai Islands, Indonesia earthquake and tsunami (see "Appendix" section). The third source applied a scaling factor of 2.55 to the finite fault slip distribution and was determined by scaling modeled wave heights from the unscaled finite fault source to match the measured leading wave amplitude at DART 43413.

Sources 4 and 5 are based on an inversion of the tsunami water level time series recorded at DART 43413 by modeling 'unit' tsunamis generated from 1 m of coseismic slip on each of 50 subfaults

(20 × 16 km). Strike and dip angles, location, depth, and rigidity values (depth-dependent, ranging from 3.12×10^{10} to 6.75×10^{10} N/m²) of the sub-faults were adopted from the USGS finite-fault source, and the rake angle was fixed to 90° (for maximum vertical displacement). The slip distribution is determined by summing scaled individual wave-forms and using a linear optimization algorithm (MATHWORKS 2012) that results in the smallest least-square difference to the measured tsunami time series. Dispersive effects were taken into account only in the form of arrival time corrections applied to each source waveform

using the fully dispersive linear wave speed (e.g., DEAN and DALRYMPLE 1991) to determine the "proper" arrival time. Source 4 was constrained by the moment magnitude ($M_w \sim 7.35$, as reported by CMT) while source 5 was not constrained and was equivalent to a slightly larger M_w of 7.43. As indicated in Fig. 6, the location of the high-slip area compares well to that of the USGS seismic inversion. A sixth source model was based on a 60 × 30-km rectangular fault plane with an average slip of 2.2 m. The fault dimensions are based on the aftershock area and the slip amount computed from the seismic
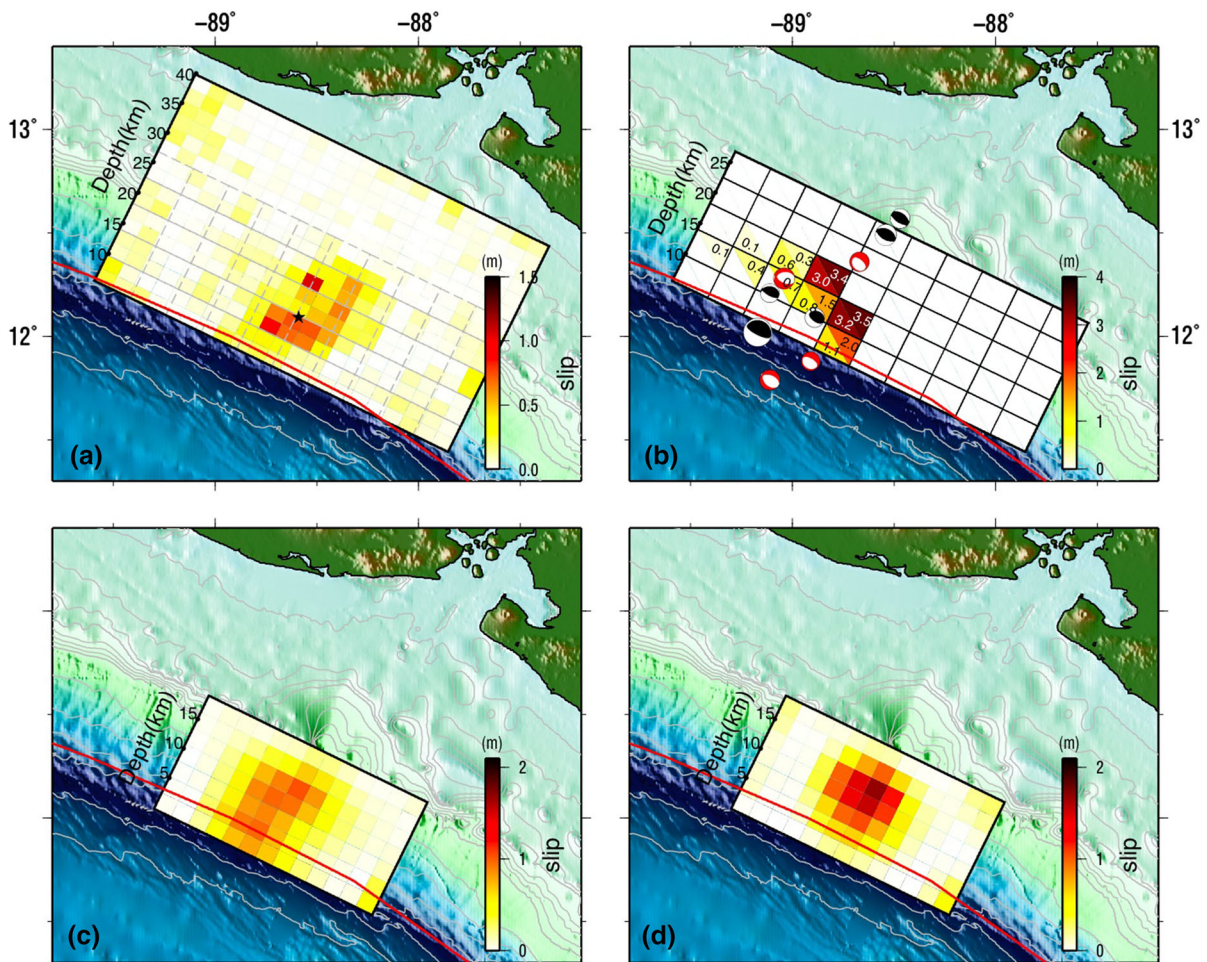

Figure 6
Slip distribution for **a** the USGS finite-fault solution (S1), **b** the solution derived from the moment magnitude constrained (S4, *lower left triangles*) and unconstrained (S5, *upper right triangles*) tsunami source inversions, **c** the YE *et al.* (2013) (S7) and **d** the modified YE *et al.* (2013) (S8) finite-fault solutions. The distribution and fault mechanism of the main and significant aftershocks from the CMT catalog are also shown. Focal-mechanism diagrams are scaled with earthquake magnitude with the largest and smallest corresponding to the main shock (M_w 7.3) and an M_w 4.8 earthquake. Normal faulting events are drawn in *red*. *Black star* in **a** indicates the location of the USGS-determined main shock epicenter
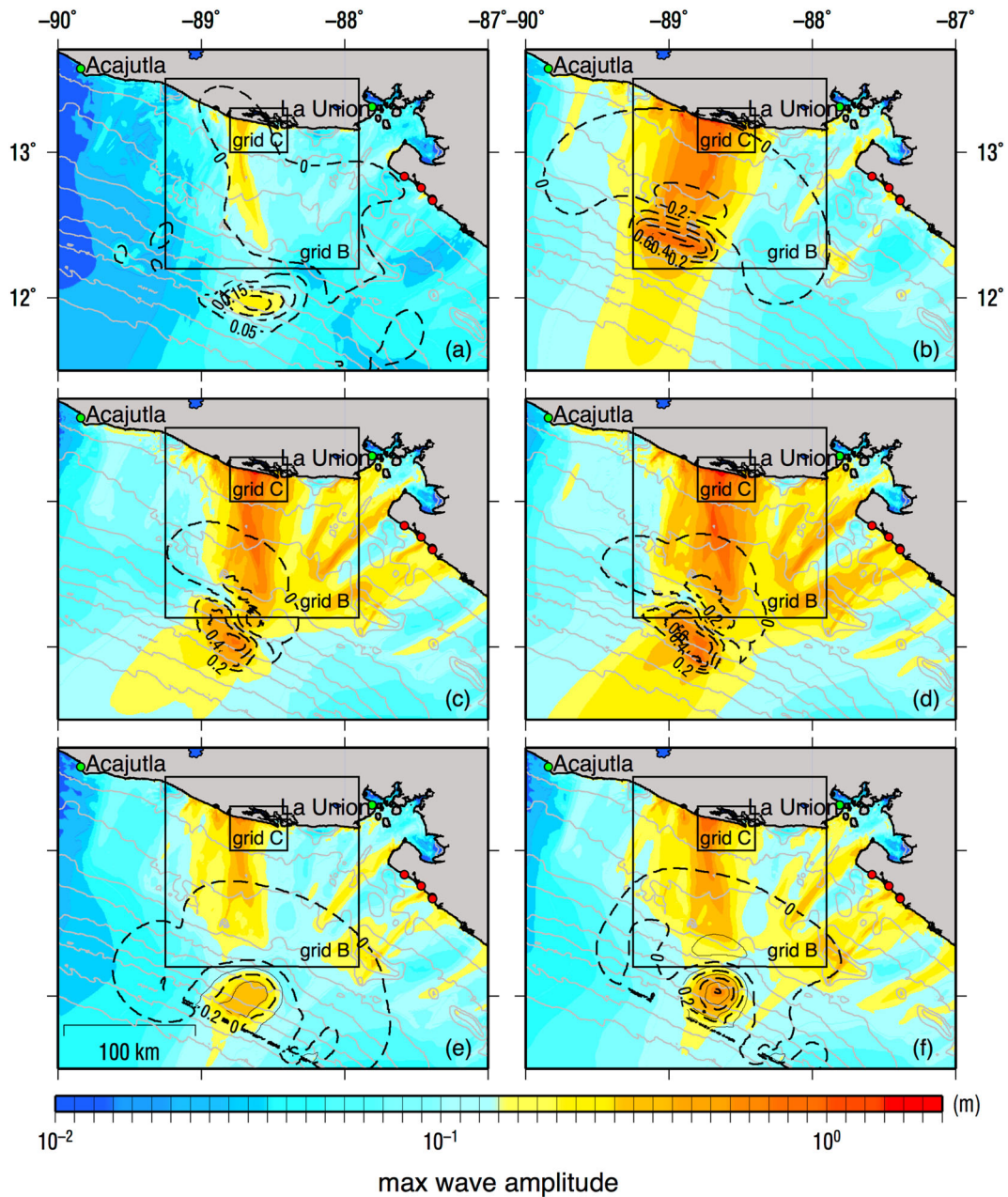
Figure 7

Modeled maximum tsunami wave heights for **a** the unscaled USGS finite-fault solution (S1), **b** rectangular fault plane with uniform slip (S6), **c** the magnitude constrained (S4), **d** the unconstrained (S5) tsunami inversion solutions, **e** the YE *et al.* (2013) (S7), and **f** the modified YE *et al.* (2013) (S8) finite-fault solutions. *Dashed lines* show contours of the static deformation. Grid A area is shown in Fig. 9. *Plots for sources S2 and S3 (the linearly-scaled finite-fault distribution) are included as supplemental figures*

moment, and was used by HEIDARZADEH and SATAKE (2014) to model the tsunami response at near- and far-field tide gauges.

Finally, we consider two models based on the teleseismic-derived finite-fault source of YE *et al.*

(2013). The source area is 130×70 km, discretized in 10×10 km subfaults. Strike and dip angles of the fault were fixed to 296° and 16°, respectively, the rake angle is variable, and the hypocenter was set at 12 km (at the center of the
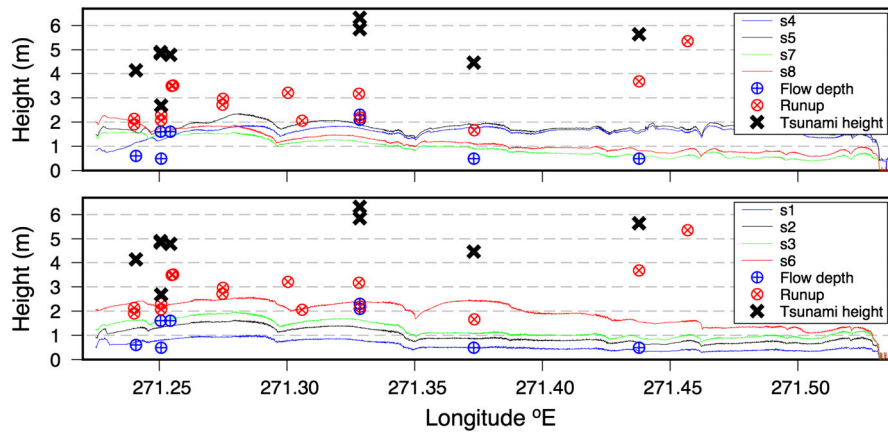
Figure 8
Tsunami heights modeled on land from the eight different sources compared to field measurements
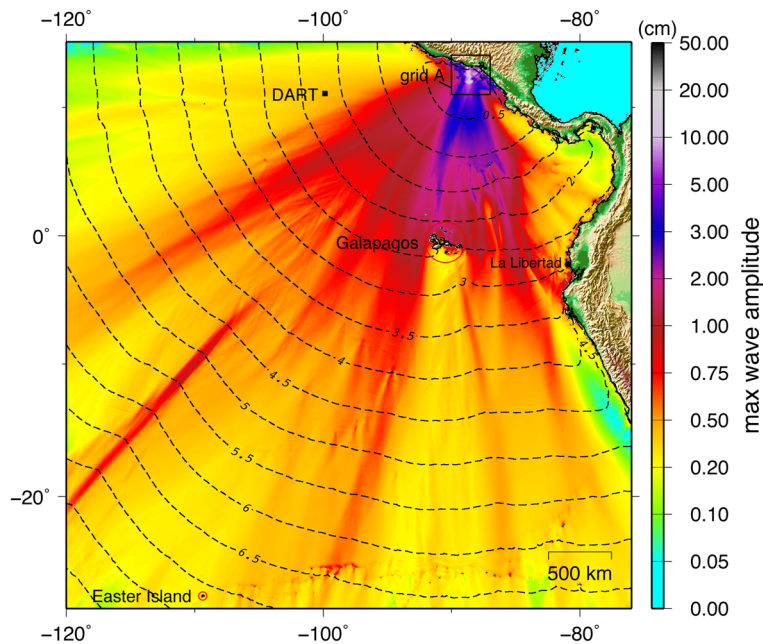

Figure 9
Modeled far-field maximum wave heights using the unscaled USGS finite-fault solution as a tsunami source. *Dashed contours* indicate tsunami travel time in hours

fault rupture area). The fault rupture area is significantly smaller than the USGS finite-fault source, allowing for more slip for a given seismic moment. Source 7 corresponds to the mechanism presented in Yᴇ *et al*. (2013), which used a rupture velocity of 2 km/s in the seismic inversion. Source 8 has the rupture velocity set to 1.5 km/s (T. Lay, *pers comm.*) resulting in a source with a nearly

equivalent seismic moment, but with more slip concentrated in a smaller area.

7. Model Results and Discussion

In the near field, the model results show strong focusing of wave energy toward the western end of
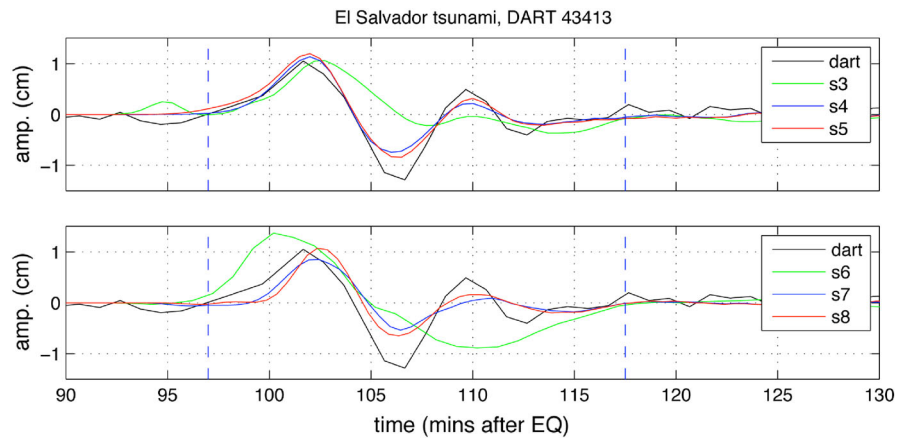
Figure 10
Recorded water level time series at DART 43414 compared to model results for six different tsunami sources. The *vertical dashed lines* denote the portion of the data record used to invert for tsunami sources *4* and *5*

the San Juan del Gozo Peninsula (Fig. 7). This feature is present in all of the modeled sources and is caused by bathymetric focusing. The beam of energy coincides with the section of the coast that experienced the strongest tsunami effects. For all of the cases, the computed tsunami heights on land (Fig. 8) are deficient relative to measured tsunami heights of 2–5 m. This deficiency may partly be a result of fine-scale bathymetric features that are not resolved in the model bathymetry and topography. The rectangular fault model (Source 6) produces the overall highest tsunami height distribution, although it is smaller than the two DART inverted and the two YE et al. (2013) sources towards the eastern end of the survey area. The scaled USGS finite-fault models result in the greatest underprediction of the measured tsunami heights. Even when scaled by a factor of 2.55 (to match the peak leading wave amplitude at DART 43413) the high-slip areas are relatively small compared to the other sources.

The simulated maximum far-field wave height distribution from the initial condition based on the unscaled USGS finite-fault solution (Fig. 9) shows a concentrated beam of wave energy directed towards the Galapagos Islands, with strong secondary beams of energy heading towards Ecuador and northern Peru. This is a feature that is present in all of the far-field simulations regardless of the source model, however, we did not explore the details of the model

results at far-field tide gauge stations. As expected, the sources based on the inversion of the DART record provide a better fit to the measured time series (Fig. 8). However, the amplitude of the wave trough could not be matched using shallow dipping thrust faults as initial conditions. These sources also show the most pronounced focusing of wave energy towards northern Nicaragua, where the tsunami caused small-scale inundation. Inspection of Fig. 10 clearly shows that the predicted wave forms from the USGS teleseismically-derived source and the rectangular fault model have a noticeably longer period than the measured data. This is not the case with the two YE et al. (2013) sources, which produce a waveform at the DART station with a comparable wavelength to the tsunami recording.

The fact that the direct application of the USGS Finite Fault model as an initial condition for the tsunami hydrodynamics yields deficient results should not come as a surprise. Indeed, in the case of the 2010 Mentawai Islands earthquake and tsunami, hydrodynamic simulations initialized with a direct application of the finite-fault slip amounts also severely underpredicted the observed wave heights (HILL et al. 2012). In order to match the observed wave effects, it was necessary to scale the slip amounts by an average value of 5.6 (NEWMAN et al. 2011). Applying the same scaling technique here, however, still results in deficient model results.

Scaling the finite-fault solution with a greater factor (2.55) produces the correct positive amplitude at the DART station, but does not significantly improve the near-field results.

The rectangular fault model produced the closest match to the measured tsunami heights in El Salvador, but it does not appear to project sufficient wave energy toward Nicaragua to explain the tsunami effects there. Additionally, the period of the modeled signal at DART 43413 from this source has a much longer period than the measured tsunami, although it matches the leading wave amplitude. The YE et al. (2013) teleseismically-derived sources compare well to the DART recording, in terms of matching the first crest amplitude and wavelength, but the inundation modeling results show that they are deficient in terms of tsunami heights in the near field. Source 8, which produces a more concentrated slip due to the lower modeled rupture velocity, matches the tsunami observations better than source 7.

A more vexing problem is the inability of the models to match the tsunami wave trough seen on the DART record. A possible explanation for the pronounced trough is that the tsunami was partially generated by the release of gravitational potential energy, as suggested by MCKENZIE and JACKSON (2012) for tsunami earthquakes with normal faulting aftershocks, such as was the case in this event (see Fig. 6b—CMT catalogue, normal faulting aftershock magnitudes ranged from M_w 4.9 to M_w 5.3). A second possible explanation for the missing trough is the lack of wave generation by horizontal motion of the sea floor. However, calculations indicate that the amplitude associated with this mechanism is one order of magnitude less than the vertical motion component (TANIOKA and SATAKE 1996). Of course, an ad-hoc landslide source could always be used to explain the DART discrepancy. It should be noted that the period of the leading tsunami wave is on the order of 6–7 min, and thus requires a highly spatially-resolved source model, which may not be possible or justified in this and similar earthquakes. The short period also indicates that frequency dispersion should modify the waveform, and this effect is neglected in the shallow-water MOST model. Lastly, the data from DART 43413 used to derive candidate source mechanisms is not ideal, since the tsunameter was located outside the main and secondary beams of tsunami energy propagation.

8. Summary and Conclusions

The earthquake of 27 August 2012 offshore of El Salvador and Nicaragua generated a tsunami with peak run-up of 5.4 m and a maximum tsunami height of 6.3 m, as measured during a post-event field survey of the affected area. The tsunami run-up was generally in the 3-m range with consistent 150 m of inundation along a 25-km stretch of largely uninhabited coastline along the San Juan del Gozo peninsula. Seismological analysis of the earthquake revealed 'slow' rupture characteristics commonly associated with enhanced tsunami effects, and this event was indeed a tsunami earthquake. A numerical modeling analysis of the tsunami using different tsunami source models highlights the difficulties encountered in accurately modeling relatively small events, particularly in the absence of accurate nearshore bathymetry or detailed onshore topography. The modeling effort was further complicated by the unusual nature of the earthquake source mechanism.

Each of the tested models produced wave focusing in the direction of the area that experienced the strongest tsunami effects, however, the computed run-up heights were lower than the measured tsunami heights. While the simplest rectangular, uniform slip source provided the highest modeled tsunami heights on shore, the distribution of modeled tsunami heights was better represented using a source model derived by inverting the tsunami wave form recorded on a nearby DART tsunameter. The preliminary USGS source model derived from teleseismic observations did not adequately capture either the near-field run-up and tsunami heights or the size and character of the signal measured at the DART station. The YE et al. (2013) teleseismically-derived sources produced tsunami signals comparable to the DART recoding and somewhat larger nearfield tsunami heights than the scaled USGS source, but were still deficient compared to the field measurements.

The fact that this was the second tsunami in this region in 20 years caused by a slow earthquake highlights the hazard posed by such events there. Hazard mitigation efforts in Central America should be sure to include information highlighting the tsunami threat from earthquakes that do not 'feel' strong

by including factors such as the duration or perceived character of the ground motion.

Acknowledgments

Appendix

For Source 2, we use a scaling approach similar to that used in NEWMAN *et al.* (2011) for the 2010 earthquake and tsunami in the Mentawai Islands offshore Sumatra, Indonesia. Following this, an appropriate scaling parameter for the displacement along the fault plane can be determined from the following relationship:

$$D/D_0 = (V_{S-ref}/V_S)^2, \qquad (1)$$

where D/D_0 is the ratio of the scaled to original slip, V_{S-ref} is a reference shear wave velocity for the region where the earthquake occurred, and V_S is the actual shear wave velocity deduced from teleseismic observations of the event and is calculated from the earthquake rupture velocity (V_R) by assuming that $V_S = 1.25\ V_R$. In general, since V_R can be highly variable, individual V_S values are calculated for each subfault in the finite fault solution, However, inspection of the finite fault model from this event reveals a consistent rupture velocity (V_R) of approximately 2.25 km/s, yielding a shear wave velocity (V_S) 2.81 km/s. From the Crust 2.0 model (BASSIN *et al.* 2000) used in the finite fault analysis, the V_{S-ref}

along the sections of greatest slip is assumed to be 3.9 km/s. Using these values in Eq. 1 leads to an average scale factor of 1.92. We note that this factor is much less than what was deduced from the 2010 Mentawai event where rupture velocities in the main slip zones were often around 1.5 km/s. In using this approach, we emphasize that this is only a first-order approximation, as pointed out in NEWMAN *et al.* (2011). This is primarily due to the fact that seismic excitation at teleseismic distances includes some upper-plate signal that cannot be fully deconvolved leading to an overamplification of the result. Secondly, because the solution is entirely based on the square of the determination of rupture velocity, any inaccuracies in the solution of V_R can have a very large impact on the final scale factor.

REFERENCES

ABE, K., TSUJI, Y., IMAMURA, F., KATAO, H., IIO, Y., SATAKE, K., BOURGEOIS, J., NOGUERA, E., and ESTRADA, F. (1993), *Field Survey of the Nicaragua Earthquake and Tsunami of September 2, 1992*, Bulletin of the Earthquake Research Institute of the University of Tokyo (in Japanese), *68*, 23–70.

ÁLVAREZ-GÓMEZ, J. A., ANIEL-QUIROGA, Í., GUTIÉRREZ-GUTIÉRREZ, O. Q., LARREYNAGA, J., GONZÁLEZ, M., CASTRO, M., GAVIDIA, F., AGUIRRE-AYERBE, I., GONZÁLEZ-RIANCHO, P., and CARREÑO, E. (2013), *Tsunami hazard assessment in El Salvador, Central America, from seismic sources through flooding numerical models*, Natural Hazards and Earth System Science, *13*, 2927–2939. doi:10.5194/nhess-13-2927-2939.

BASSIN, C., LASKE, G., and MASTERS, G. (2000), *The Current Limits of Resolution for Surface Wave Tomography in North America*, EOS Trans AGU, *81*, F897.

BOATWRIGHT, J., and CHOY, G. L. (1986), *Telesesismic estimates of the energy radiated by shallow earthquakes*, Journal of Geophysical Research-Solid Earth and Planets, *91*(B2), 2095–2112.

BORRERO, J. C. (2012), Field Survey Report of Tsunami Effects Caused by the August, 2012 Offshore El Salvador Earthquake, UNESCO/IOC report.

CONVERS, J. A., and NEWMAN, A. V. (2011), *Global Evaluation of Large Earthquake Energy from 1997 Through mid-2010*, J. Geophys. Res., *116*, B08304, doi:10.1029/2010JB007928.

DEAN, R. G., and DALRYMPLE, R. A., Water Wave Mechanics for Engineers and Scientists (World Scientific, Teaneck, NJ, 1991).

FERNANDEZ, M., ORTIZ-FIGUEROA, M., and MORA, R. (2004), Tsunami Hazards in El Salvador, in Rose, W., Bommer, J., Lopez, D., Carr, M., and Major, J. eds. Natural Hazards in El Salvador, Boulder Colorado. Geological Society of America, Special Paper 375. pp. 435–444.

HEIDARZADEH, M., and SATAKE, K. (2014), *The El Salvador and Philippines tsunami of August 2012: insights from sea level data analysis and numerical modeling*. Pure and Applied Geophysics. doi:10.1007/s00024-014-0790-2

Hill, E, Borrero, J., Huang, Z., Qiu, Q., Banerjee, P., Natawidjaja, D., Elosegui, P., Fritz, H., Pranantyo, I., Li, L., Macpherson, K., Skanavis, V., Synolakis, C., and Sieh, K. (2012), *The 2010 Mw 7.8 Mentawai earthquake: Very shallow source of a rare tsunami earthquake determined from tsunami field survey and near-field GPS*. Journal of Geophysical Research, Vol *117*, B06402, doi:10.1029/2012JB009159.

Houston, H. (2001), *Influence of depth, focal mechanism, and tectonic setting on the shape and duration of earthquake source time functions*, J. Geophys. Res.-Solid Earth, *106*(B6), 11137–11150.

Ji, C., Wald, D. J. and Helmberger, D. V. (2002), *Source description of the 1999 Hector Mine, California earthquake; Part I: Wavelet domain inversion theory and resolution analysis*, Bull. Seism. Soc. Am., Vol *92*, No. 4. pp. 1192–1207.

Kanamori, H. (1972), *Mechanism of Tsunami Earthquakes, Physics of the Earth and Planetary Interiors*, *6*, 346–359.

Kanamori, H. and Kikuchi, M. (1993), *The 1992 Nicaragua earthquake: a slow tsunami earthquake associated with subducted sediments*. Nature, *361*, 714–716.

Kelleher, J. A. (1972), *Rupture zones of large South-American earthquakes and some predictions*, J. Geophys. Res., *77*(11), 2087–2103, doi:10.1029/JB077i011p02087.

Lynett, P., Weiss, R., Renteria, W., De La Torre Morales, G., Son, S., Arcos, M. and MacInnes, B. (2013), *Coastal Impacts of the March 11th Tohoku, Japan Tsunami in the Galapagos Islands*. Pure Appl. Geophys. *170*(6–8):1189–1206, doi:10.1007/s00024-012-0568-3.

MATLAB and Statistics Toolbox Release 2012, The MathWorks, Inc., Natick, Massachusetts, United States.

McKenzie, D., and Jackson J. (2012), *Tsunami earthquake generation by the release of gravitational potential energy*, Earth and Planetary Science Letters, 345–348, 1–8.

Newman, A. V., Hayes G., Wei Y., and Convers J. (2011), *The 25 October 2010 Mentawai tsunami earthquake, from real-time discriminants, finite-fault rupture, and tsunami excitation*, Geophys. Res. Lett., *38*, L05302, doi:10.1029/2010GL046498.

Newman, A. V., and Okal, E. A. (1998), *Teleseismic estimates of radiated seismic energy: The E/M0 discriminant for tsunami earthquakes*, J. Geophys. Res., *103*, 26885–26898.

Okada, Y. (1985), *Surface deformation due to shear and tensile faults in a half-space*, Bulletin of the Seismological Society of America, *75*, 1135–1154.

Satake, K., Bourgeois, J., Abe, K., Abe, K., Tsuji, Y., Immura, F., Iio, Y., Katao, H., Noguera, E., and Estrada, F. (1994), *Tsunami Field Survey of the 1992 Nicaragua Earthquake*, Eos: Trans. Am. Geophys. Un. 74,13, pp 145, 156–157.

Synolakis, C. E., and Okal, E. A. (2005), 1992–2002: Perspective on a decade of post-tsunami surveys, in: Tsunamis: Case studies and recent develop- ments, ed. K. Satake, Adv. Nat. Technol. Hazards, 23:1–30.

Tanioka, Y., and Satake, K. (1996), *Tsunami generation by horizontal displacement of ocean bottom*, Geophysical Research Letters, Volume *23*, Issue 8, pp. 861–864.

Titov, V., and González, F. I. (1997), Implementation and testing of the Method of Splitting Tsunami (MOST) model, NOAA Tech. Memo. ERL PMEL-112 (PB98-122773), 11 pp., Pac. Mar. Environ. Lab., NOAA, Seattle, Wash.

UNESCO (2013), International Tsunami Survey Team (ITST), Post-Tsunami Survey Field Guide. 2nd Edition. Dominey-Howes, D. and Dengler, L. eds., IOC Manuals and Guides No. 37, Paris: (English).

US Geological Survey (2012), http://earthquake.usgs.gov/earthquakes/eqinthenews/2012/usc000c7yw/finite_fault.php.

White, R. A., Lígoria, J. P., and Cifuentes, I. L. (2004), "Seismic history along the Middle America subduction zone along El Salvador, Guatemala and Chiapas, Mexico: 1526-2000". In Rose, William Ingersol (et al.) (Eds). Natural Hazards in El Salvador. Geological Society of America, Special Paper 375. pp. 379–96. ISBN:0-8137-2375-2.

Ye, L., Lay T., and Kanamori, H. (2013), *Large earthquake rupture variations on the Middle America megathrust*, Earth and Planetary Science Letters, *381*, pp. 147–155.